Full length article

First-principles design of highly-efficient earth-abundant electrocatalysts for hydrogen evolution reaction: TiF$_3$ and its analogs

Junru Wang, Siyun Qi, Xiaohan Song, Yuanyuan Qu, Weifeng Li, Mingwen Zhao*

School of Physics & State Key Laboratory of Crystal Materials, Shandong University, Jinan 250100, Shandong, China

A B S T R A C T

Hydrogen evolution reaction (HER) plays an important role in water splitting to produce hydrogen. The high price of precious platinum-based catalysts that are the best HER electrocatalysts by now hampers the commercial application. Low-cost, earth-abundant and highly-efficient HER electrocatalysts are thus long-desired. On the basis of first-principles calculations, we investigated the HER electrocatalytic performance of the non-precious TiF$_3$ and its analogs. Our calculations showed that TiF$_3$ and WO$_3$ can serve as efficient HER electrocatalysts with the overpotentials comparable to those of the platinum-based catalysts. To uncover the origins of electrocatalytic performance, we established a relationship between the surface adsorption ability of a material and its electronic structure. The low HER overpotentials, unique porous structure and high abundance in earth make these materials promising candidates for high-performance HER electrocatalysts.

1. Introduction

Increasing environmental issues and depletion of fossil fuels have posed urgent demands on clean and renewable energy sources [1]. Hydrogen evolution reaction (HER) which is a fundamental process in electrocatalysis plays an important role in energy conversion through water splitting to produce hydrogen [2]. An ideal HER electrocatalyst should have zero overpotential. But the realistic electrocatalytic materials always have a nonzero overpotential that is needed to overcome the initial reaction energy barrier. Therefore, it's vital to design the catalysts with a low overpotential and fast kinetics for the efficient HER [3]. By far, noble metal Pt and Pt-group metals were adopted as the most reactive HER electrocatalysts [4,5]. However, the low abundance and high cost limit their widespread utilization. Development of low-cost, earth-abundant, high-efficient electrocatalysts to replace Pt-based electrocatalysts is highly demanding and has become the frontier of catalysis research.

A variety of non-noble metal catalyst systems have recently brought up and emerged as promising candidates for new-generation electrocatalysts. These materials include transition metal chalcogenides MX$_2$ (M: Mo, W, Fe; X: S, Se) [6–10], metal carbides [11], metal nitrides [12], metal phosphide [13], metal oxide [14], Mxene [15], metal-free material (carbon material and C$_3$N$_4$) [16–18] and metal materials (Ni, Co, etc.) [19]. However, the HER efficiency of the electrocatalysts remains lower than the noble metal electrocatalysts. Additionally, some

of the HER catalysts face the problem of irreversible recovery due to structure deformation as more active sites are introduced, e.g. by forming porous structures on surfaces [20].

In this work, we proposed a new family of HER electrocatalytic materials: TiF$_3$ and its analogs with intrinsic large voids in its cubic crystal [21]. Using first-principles calculations, we demonstrated that the under-coordinated metal atoms on the surfaces exhibit excellent HER catalytic performance. The predicted overpotentials of these non-noble metal catalysts are comparable to those of the Pt-based catalysts. We also developed a description for the relationship between bond strength and electronic structure. We hope that this work can unlock the potential of earth-abundant materials as highly-efficient HER electrocatalysts and offer vital guidance for the design of novel HER electrocatalysts.

2. Method and computational details

Our first-principles calculations were performed within the framework of density-functional theory (DFT), which is implemented in the Vienna ab initio simulation package known as VASP [22]. The electron–ion interactions were described by projector-augmented-wave (PAW) potentials [23]. The generalized gradient approximation (GGA) [24] in the form of Perdew–Burke Ernzerhof (PBE) [25] was adopted for the exchange–correlation functional. The plane waves employed to expand the Kohn–Sham electron wavefunction have an energy cutoff of

520 eV. Structural optimizations were carried out using a conjugate gradient (CG) method without any symmetry constrains until the maximum force on each atom was less than 0.01 eV Å^{-1}. In the electronic band structure calculations, we employed the hybrid functional proposed by Heyd, Scuseria and Ernzerhof (HSE06) [26]. In the HSE06 functional, the PBE exchange term is splitted into a short-range and a long-range part, and 25% of the short-range part is then replaced by a short-range Hartree-Fock term. The Brillouin zone (BZ) integration was sampled on a grid of $11 \times 11 \times 11$ *k*-points for the unit cells of bulk crystals [27]. The long-range van der Waals interactions were taken into account by using the DFT-D2 method [28]. For the nanosheets, a 2×2 slab repeated periodically along the *x*- and *y*-directions was employed and a vacuum space up to 20 Å was applied along the *z*-direction to avoid interaction between neighboring images. A $5 \times 5 \times 1$ *k*-point grid for structural optimizations, a $9 \times 9 \times 1$ *k*-point grid for static computation, and a $21 \times 21 \times 1$ *k*-point grid for the density of states (DOS) calculations were employed in the Brillouin zone integration [27]. The slab model contains three atomic layers with two symmetric terminals. The top two layers were fully relaxed during structural optimizations, while other layers were fixed at the lattice positions of bulk crystals. Spin-polarization was considered in the whole calculations. The kinetic barrier and transition state for H desorption and H_2 formation were simulated by using the climbing image nudged elastic band (CNEB) method as implemented in the VASP transition state tools [29,30]. The intermediate images were relaxed until the forces were less than 0.02 eV/Å.

As for the HER in an acid electrolyte (pH = 0), H^+ can act as the proton donor, the overall reaction scheme can be written as:

$$H^+ + e^- + * \rightleftharpoons 1/2H_2 * \rightleftharpoons 1/2H_2(g) + * \tag{1}$$
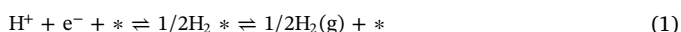
The symbol * represents the catalysts and H* is the H adsorbed on the surface of the catalysts. The free energies of the studied systems can be obtained by using the following equation: $\Delta G = \Delta E + \Delta ZPE - T\Delta S$, where ΔE, ΔZPE, ΔS are the binding energy, zero-point energy change and entropy difference. ΔZPE is the zero-point energy difference between the adsorbed state of the system and the gas-phase state. The reversible hydrogen electrode (RHE) model developed by Nørskov and co-workers was used to obtain the Gibbs reaction free energy of these electrochemical elementary steps [31,32]. In this model, we set up RHE as the reference electrode where the proton-electron pair corresponds to half a hydrogen molecule: $\mu_{H+} + \mu_{e^-} = 1/2\mu_{H2}$, at conditions of U = 0 V and P_{H2} = 1 bar.

The chemical potential of each adsorbate is defined as: $\mu = E + E_{ZPE} - T \times S$, where E is the total energy obtained from DFT calculations, E_{ZPE} is zero-point energy correction calculated from vibrational frequencies, and S is the entropy at 298 K taken from the standard tables.

The reaction free energy (ΔG_{H*}) and the theoretical overpotential (η) of HER are determined by using the following equations:

$$\Delta G_{H*} = \mu_{H*} - 0.5 \times \mu_{H_2} - \mu_*$$

$$\eta = -|\Delta G_{H*}|/e$$

For the calculations of the band center of the anti-bonding state projected onto the d orbitals of transition metal atom and s orbitals of the H atom ($E_{anti\text{-}bond}$), the following expression was used [33]:

$$E_{anti-bond} = \frac{\int_{E_f}^{+\infty} E \times (\rho_d(E) + \rho_s(E))dE}{\int_{E_f}^{+\infty} (\rho_d(E) + \rho_s(E))dE}.$$

3. Results and discussion

The crystal structures of TiF_3 and its analogs (WO_3, ScF_3, ReO_3, NbF_3, TaF_3, and MoF_3) have a cubic cell belonging to a space group of pm$\bar{3}$m. Metal ions locate at the corners of the cube linked by anions. Each metal ion is coordinated by six anions, and each anion is bonded to two metal ions. The optimized lattice constants range from 3.795 Å

Table 1
Lattice constants and electronic properties of TiF_3 and its analogs. The band gaps were obtained by using the HSE06 functional.

	WO_3	ScF_3	ReO_3	TiF_3	NbF_3	TaF_3	MoF_3
Lattice constant (Å)	3.834	4.068	3.795	3.933	4.112	4.110	4.053
Magnetic moments (μ_B/cell)	0	0	0	1	2	2	3
Band Gap (eV)	1.468	8.638	0	Half-metal	Half-metal	Half-metal	2.632

to 4.112 Å, as listed in Table 1. Such a line-centered cubic lattice leads to intrinsic large voids, offering abundant active sites and channels for hydrogen diffusion. Notably, the TiF_3 material and its analogs have been synthesized more than half a century ago [34–41]. Very recently, their utilizations in hydrogen storage and photocatalysis were reported [42,43]. TiO_2/TiF_3 hybrids exhibit excellent visible-light photocatalytic reactivity in the photodegradation of methyl orange under visible light irradiation, which was attributed to the high concentration of Ti^{3+} species provided by TiF_3 [42]. TiF_3 can also act as an efficient catalyst to facilitate hydrogen and dehydrogenation in a variety of reversible hydrogen storage materials, such as MgH_2 and $NaAlH_4$ [43]. Although the associated mechanism remains under debate, the interaction between TiF_3 and hydrogen is expected to play an important role in the catalytic processes. However, the electrocatalytic HER performance of TiF_3 in water splitting to produce hydrogen has never been reported to date.

These materials exhibit diverse electronic properties. TiF_3 crystal has a spin-polarized ground state with remarkable spin-splitting of about 1.4 eV, as shown in Fig. S1(b). Each Ti ion owns ~1 μB magnetic moments. Half-metallicity is quite evident in the band structure of TiF_3 crystal. The Fermi level crosses the bands of one spin channel, leading to abundant electronic states at the Fermi level, whereas a large band gap of about 8.00 eV appears in the opposite spin channel. The bands in the proximity of the Fermi level are rather dispersive in the momentum space, suggesting good conductivity of the conducting spin channel. The origin of the electron spin-polarization has been reported in our previous work [44]. Electron spin-polarization has also been found in the electronic band structures of NbF_3, TaF_3 and MoF_3 crystals. Similar to the case of TiF_3, NbF_3 and TaF_3 are half-metals and each metal ion owns ~2 μB magnetic moments. MoF_3 is a spin-polarized semiconductor where each Mo ion carries ~3 μB magnetic moments. No spin-polarization was found in ScF_3, WO_3, and ReO_3 crystals. The electronic structures of these materials are summarized in Fig. S1.

In these line-centered cubic lattices, the (001) surfaces have the lowest density of dangling bonds and thus are more accessible in experiments. The energetic preferability of the (001) surfaces was also been confirmed by the surface energy calculations, as seen in Table S1. In the work, we choose the (001) surface of these materials to investigate the ability of hydrogen adsorption. A slab model of a 2×2 nanosheet terminated by two (001) planes was adopted, as shown in Fig. 1(a). The slab lattice parameters were fixed to the optimized cell parameters of bulk crystals, to mimic the support bulk. For simplification, the nanosheets contain only three atomic layers with the atoms on the lowest layer been fixed to mimic bulk effect. We also checked the convergence of this model by employing a thicker model contains more atomic layers and got the same conclusion, as shown in Fig. S2.

Now we take the TiF_3 nanosheet as a representative model to describe the adsorption of hydrogen on the (001) plane of these materials. The possible adsorption sites include the center of a square (H site), the top of a Ti atom (T1 site) or an F atom (T2 site), and the top of a Ti−F bond (B site), as shown in Fig. 1(a). It is found that the H atom can stably adsorb on these sites expect the B site. The H atom placed at the B site moves to the T1 site during structural relaxation.

We defined the binding energy (E_b) of a H atom on the TiF_3 nanosheet as $E_b = E_{H+TiF_3} - E_{TiF_3} - E_H$, where E_{H+TiF_3}, E_{TiF_3} represent the
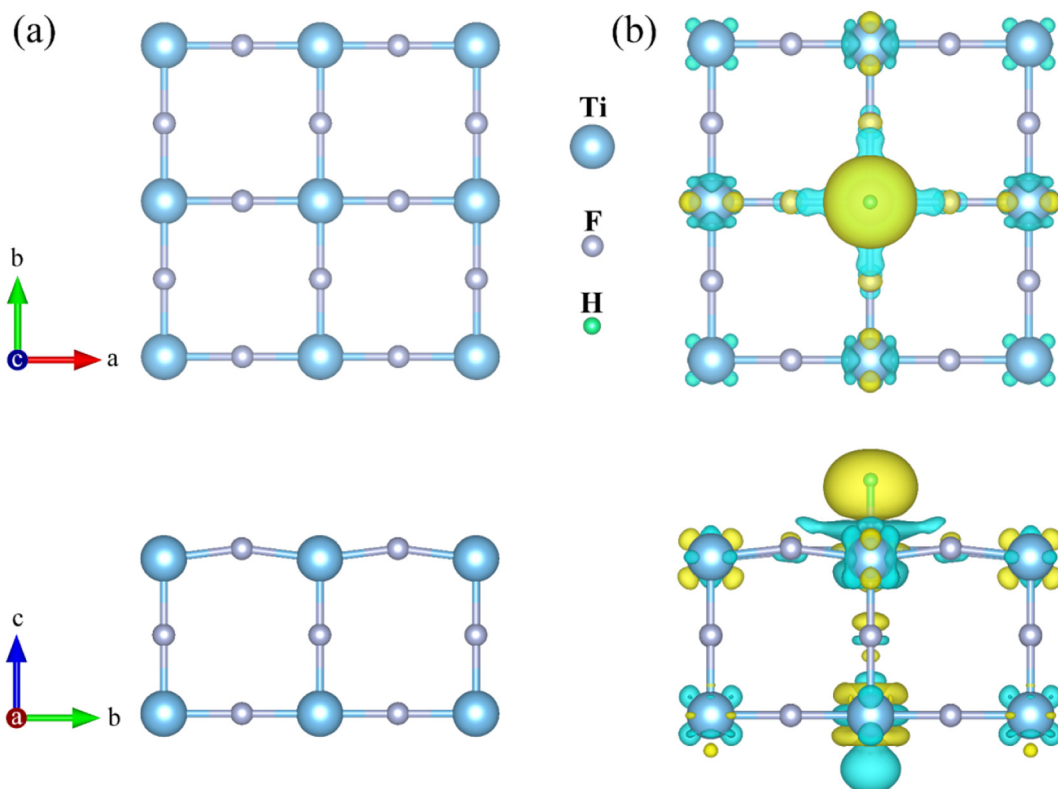
Fig. 1. (a) Top and side views of possible adsorption sites on the pristine TiF$_3$ nanosheets. (b) Differential charge densities of H adsorbed on the TiF$_3$ nanosheet. Yellow and blue colors indicate the electron accumulation and depletion, respectively. The isovalue is 0.002 e Å^{-3}. (For interpretation of the references to colour in this figure legend, the reader is referred to the web version of this article.)

total energies of TiF$_3$ nanosheets with and without H adsorption, E$_H$ is the energy of an isolated H atom. The E$_b$ values calculated from our calculations are -2.514 eV (for the T1 site), -1.871 eV (for the T2 site) and 0.485 eV (for the H site), respectively. The T1 site (top of Ti) is the energetically most preferable for H adsorption. Generally, an obvious electron-accepting region is commonly found around the H atom, representing a significant electron transfer from TiF$_3$ to H, as shown in Fig. 1(b). This is also consistent with the larger electronegativity of H than that of Ti. The amounts of electron transfer were quantitatively evaluated by performing Bader charge analysis [45]. About 0.46 electrons transfer from the TiF$_3$ nanosheets to the adsorbed H atom.

Generally, the overall HER pathway can be described by a three-state diagram comprising an initial state H$^+$ + e$^-$, an intermediate adsorbed H*, and a final product 1/2H$_2$ (Fig. 2a) [33,46–47]. The Gibbs free-energy of the intermediate state, $|\Delta G_{H_*}|$, was regarded as a major descriptor of the HER activity. A smaller $|\Delta G_{H_*}|$ means high catalytic activity. The optimal value of $|\Delta G_{H_*}|$ is zero. The well-known highly efficient Pt catalyst has $|\Delta G_{H_*}| \approx 0.09$ eV [46] (Fig. 2a). We also

calculated the $|\Delta G_{H_*}|$ of the (111) surface of Pt crystal using the above-mentioned strategy and found that it is about 0.12 eV. Notably, the HER overpotentials (η) of Pt-based electrocatalysts measured in experiments are highly dependent on the composition of the catalysts, which are -0.16 V for Pt/Ni$_3$N nanosheets [48], –0.05 V for Pt-Ni/C octahedral [49], –0.052 V for Pt/C [50], –0.022 V for Pt-Ni-Co [50], –0.032 V for Pt/Ni(OH)$_2$ [51], and -0.01 V for Pt/Fe-NF [52]. Our calculations showed that the ΔG_{H_*} of TiF$_3$ is only -0.03 eV for the T$_1$ site, which is comparable to those of Pt-based catalysts. The HER free-energy diagrams of TiF$_3$ and its analogs are plotted in Fig. 2(a). TiF$_3$ has two types of action sites, T1 and T2. The ΔG_{H_*} of T2 site is about -0.55 eV. Notably, WO$_3$ and ReO$_3$ also exhibit high HER catalytic performance with the overpotentials of only -0.05 V and -0.22 V. However, ReO$_3$ is not only as expensive as Pt but also a compound of acute toxicity, and thus unsuitable for water splitting to produce hydrogen in practical applications.

We then investigated the HER free-energy diagrams of TiF$_3$, WO$_3$ and ReO$_3$ under different H* coverage levels (θ). We considered four
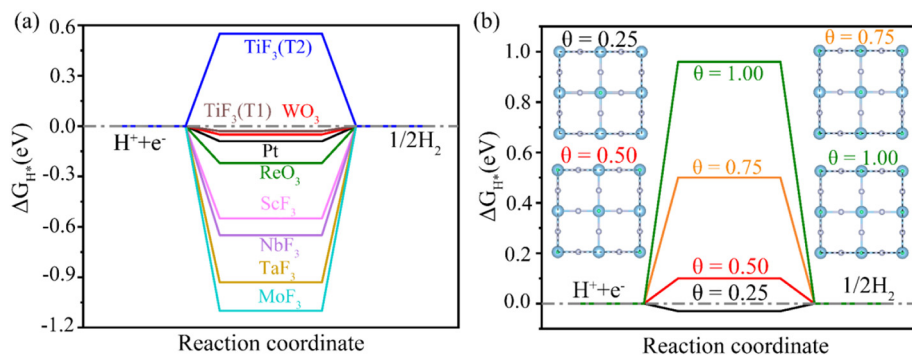
Fig. 2. (a) The calculated free-energy diagrams of HER at the equilibrium potential for TiF$_3$ and its analogs and Pt reference. (b) Free-energy diagram of HER on the surface of TiF$_3$ under different H* coverage (0.25, 0.5, 0.75, and 1.0) conditions. Blue, argent, green spheres indicate the Ti, F and H atoms, respectively. (For interpretation of the references to colour in this figure legend, the reader is referred to the web version of this article.)

levels of H* coverage with θ = 0.25, 0.5, 0.75 and 1.0, corresponding to adsorbing 1, 2, 3 and 4 hydrogen atoms on a 2 × 2 supercell. The free-energy diagrams under different H* coverage are plotted in Figs. 2(b) and S3. The ΔG_{H_*} of TiF_3 increases to 0.05, 0.17 and 0.24 eV at θ = 0.5, 0.75 and 1.0, respectively. We can see that the HER performance of TiF_3 is comparable to the Pt-catalysts as the H* coverage is lower than ~50%. For ReO_3, high HER catalytic performance is maintained at different H* coverage, as indicated by the stable ΔG_{H_*} around −0.22 eV. For WO_3, The ΔG_{H_*} of TiF_3 increases to 0.04, 0.17 and 0.26 eV at θ = 0.5, 0.75 and 1.0, it is noteworthy that the HER free energies of WO_3 and TiF_3 exhibit uniform trend with the increase of H* coverage. The stability of the ΔG_{H_*} values is crucial for maintaining high HER performance of the catalysts at different H* coverage levels.

The apparent activity of electrocatalyst materials can be improved through two strategies. One is climbing to the top of the volcano plot through optimizing ΔG_{H_*}. The other is modifying the physiochemical properties of catalysts to increase the density of the exposed active sites for an identified sample. The first strategy can be achieved through the principle that the catalytic property of a catalyst is determined by its electronic structure [53]. A descriptor was always introduced to describe the relationship between ΔG_{H_*} and electronic structure. Here, we established a descriptor based on the electron density of states (DOS) to show the relationship between ΔG_{H_*} and electronic structure. We enumerated seven relationships, as shown in Supplementary Fig. S4, and found that the weighted center of total DOS without the adsorption of H below the Fermi level (DOS2) shows a better linear relation with ΔG_{H_*} for the crystals considered in this work, as shown in Fig. 3(a). The closer the weighted center of total DOS is to the Fermi level, the stronger the H* adsorption strength will be. Considering the decisive role of d orbitals in the formation of H-M bonds, only the d-projected DOS of transition metal atom in the adsorption position is presented. The adsorption strength of hydrogen is connected to the center of the d-orbit of the underlying metal atom. As the center is closer to the Fermi level, stronger interaction between adsorbate and catalyst surface will be

obtained.

The relationship between the surface adsorption ability of a material and its electronic structure can be explained in terms of bond formation. When a proton from the electrolyte combines with an electron from the electrode on the catalyst surface to form a H*, the electronic states of the active transition metal interacts with those of hydrogen, and consequently their hybridized energy levels split into two: anti-bonding states (σ*) that is normally above the Fermi level and the bonding states (σ) under the Fermi level. The adsorption strength of H on the catalyst surface can be tuned by the position of the anti-bonding states, that is, the closer the anti-bonding states to the Fermi level, the weaker the interaction between catalyst surface and hydrogen and vice versa, as elucidated in Fig. 3(b). The occupation of anti-bonding states weakens the adsorption of the H on the catalyst surface.

The surface reconstruction of these catalysts also affects their interaction with H. TiF_3 and its analogs undergo a z-in Jahn-Teller (JT) distortion, forming a compressed octahedral structure. Therefore, the electron wavefunction overlap between the catalyst surface and H atom mainly is more remarkable along the z-direction than other directions. This is consistent with the partial spin-resolved electron density of the e_g states of the transition metal atom, (Figs. 3(c), S5) which shows that the contributions of the d_{z2} orbit are closer to the Fermi level than those of the d_{x2-y2} orbit. The energy and wavefunctions of these d_{z2} states facilitate the strong interaction with H, i.e., the closer the center of d_{z2} orbit to the Fermi level, the stronger interaction between adsorbate and catalyst surface will be obtained (Fig. S4(g)).

Finally, we discussed the catalytic performance of TiF_3 and its analogs. We found that H_2O prefers to absorb on the top of Ti (T1 site) on the surface with the binding energy of 0.67 eV. The decomposition from H_3O^+ to H^+ and H_2O is barrierless, which is beneficial for the Volmer step. We evaluated the kinetic barriers for two adsorbed H* species on the active sites of TiF_3, WO_3 and ReO_3 to form a H_2 molecule in the framework of the Tafel mechanism. In the initial state, the distances between the H atom and the active sites are 1.72 Å, 1.74 Å and
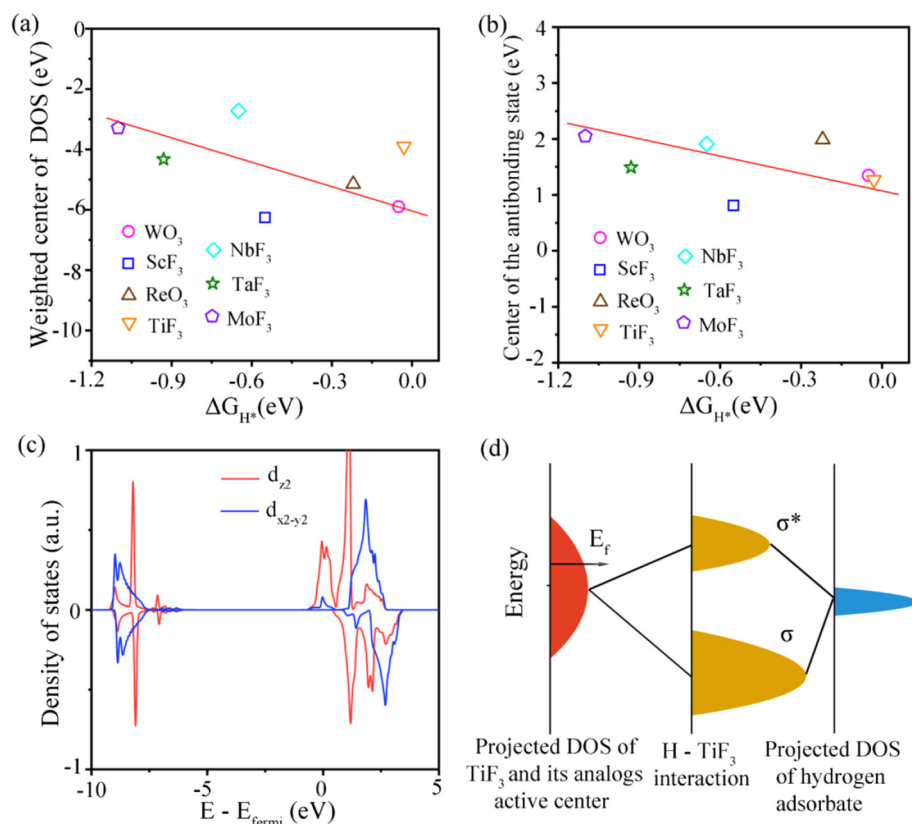
Fig. 3. (a) The relationship between ΔG_{H_*} and the weighted center of projected d-orbital density of states of transition metal atom without hydrogen adsorption. Only the occupied states are taken into accounted. (b) The center of the anti-bonding states projected on the d orbitals of transition metal atom and s orbitals of the H atom. (c) The spin-resolved electron density of the e_g states projected onto the Ti on the surface of TiF_3. (d) Energy level diagram of orbital hybridization of active sites and hydrogen adsorbate. E_F is the Fermi level of the substrate; σ* and σ indicate bonding and anti-bonding states, respectively.
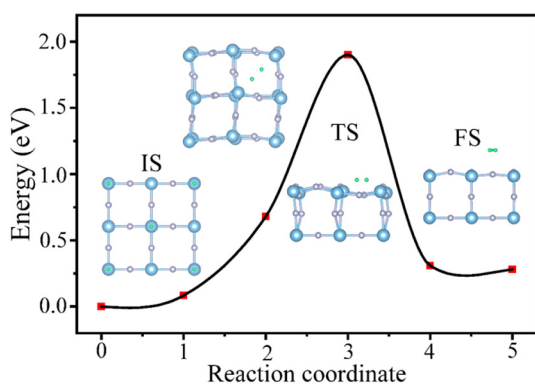
Fig. 4. Free energy profiles of Tafel mechanism pathway for hydrogen evolution on TiF$_3$.

1.67 Å for TiF$_3$, WO$_3$ and ReO$_3$, respectively. The energy barriers between the initial states and the adsorbing states are determined to be 1.90 eV (TiF$_3$), 3.11 eV (WO$_3$) and 3.89 eV (ReO$_3$), respectively, as shown in Figs. 4 and S6. Notably, the energy barrier of TiF$_3$ is comparable to the values of freestanding carbon-based materials (~2 eV) [16], N-doped graphene on Fe substrate (1.93 eV) [54]. From a thermodynamic point of view, TiF$_3$ provides suitable binding strength for HER catalysis.

4. Conclusions

In summary, we proposed from first-principles calculations a new family of electrocatalytic materials with intrinsic porous structures - TiF$_3$ and its analogs, for hydrogen evolution reaction. They are predicted to have wonderful HER catalytic performance characterized by low free-energy changes, TiF$_3$ ($\Delta G_{H_*} = -0.03$ eV), WO$_3$ ($\Delta G_{H_*} = -0.05$ eV). A descriptor based on the d-band center is proposed to reveal the origins of catalytic activity. These theoretical results are expected to offer a vital guidance for the design of high-efficient hydrogen evolution reaction electrocatalysts.

Declaration of competing interest

There are no conflicts to declare.

Acknowledgement

Appendix A. Supplementary data

Supplementary data to this article can be found online at https://doi.org/10.1016/j.apsusc.2019.143623.

References

[1] M.S. Dresselhaus, I.L. Thomas, Alternative energy technologies, Nature 414 (2001) 332–337.
[2] Z.W. Seh, J. Kibsgaard, C.F. Dickens, I. Chorkendorff, J.K. Norskov, T.F. Jaramillo, Combining theory and experiment in electrocatalysis: insights into materials design, Science 355 (2017) eaad4998.
[3] J.A. Turner, Sustainable hydrogen production, Science 305 (2004) 972–974.
[4] Y. Jiao, Y. Zheng, M. Jaroniec, S. Qiao, Design of electrocatalysts for oxygen- and hydrogen-involving energy conversion reactions, Chem. Soc. Rev. 44 (2015) 2060–2086.
[5] B.E. Conway, B.V. Tilak, Interfacial processes involving electrocatalytic evolution and oxidation of H$_2$, and the role of chemisorbed H, Electrochim. Acta 47 (2002) 3571–3594.
[6] J.D. Benck, T.R. Hellstern, J. Kibsgaard, P. Chakthranont, T.F. Jaramillo, Catalyzing the hydrogen evolution reaction (HER) with molybdenum sulfide nanomaterials,

ACS Catal. 4 (2014) 3957–3971.
[7] T.F. Jaramillo, K.P. Jorgensen, J. Bonde, J.H. Nielsen, S. Horch, I. Chorkendorff, Identification of active edge sites for electrochemical H$_2$ evolution from MoS$_2$ nanocatalysts, Science 317 (2007) 100–102.
[8] R. Miao, B. Dutta, S. Sahoo, J. He, W. Zhong, S.A. Cetegen, T. Jiang, S.P. Alpay, S.L. Suib, Mesoporous Iron sulfide for highly efficient electrocatalytic hydrogen evolution, J. Am. Chem. Soc. 139 (2017) 13604–13607.
[9] G. Gao, Y. Jiao, F. Ma, Y. Jiao, E. Waclawik, A. Du, Charge mediated semiconducting-to-metallic phase transition in molybdenum disulfide monolayer and hydrogen evolution reaction in new 1T′ phase, J. Phys. Chem. C 119 (2015) 13124–13128.
[10] G. Gao, Q. Sun, A. Du, Activating catalytic inert basal plane of molybdenum disulfide to optimize hydrogen evolution activity via defect doping and strain engineering, J. Phys. Chem. C 120 (2016) 16761–16766.
[11] W. Chen, C.H. Wang, K. Sasaki, N. Marinkovic, W. Xu, J.T. Muckerman, Y. Zhu, R.R. Adzic, Highly active and durable nanostructured molybdenum carbide electrocatalysts for hydrogen production, Energy Environ. Sci. 6 (2013) 943–951.
[12] B.F. Cao, G.M. Veith, J.C. Neuefeind, R.R. Adzic, P.G. Khalifah, Mixed close-packed cobalt molybdenum nitrides as non-noble metal electrocatalysts for the hydrogen evolution reaction, J. Am. Chem. Soc. 135 (2013) 19186–19192.
[13] P. Jiang, Q. Liu, X. Sun, NiP$_2$ nanosheet arrays supported on carbon cloth: an efficient 3d hydrogen evolution cathode in both acidic and alkaline solutions, Nanoscale 6 (2014) 13440–13445.
[14] R. Wu, J. Zhang, Y. Shi, D. Liu, B. Zhang, Metallic WO$_2$–carbon mesoporous nanowires as highly efficient electrocatalysts for hydrogen evolution reaction, J. Am. Chem. Soc. 137 (2015) 6983–6986.
[15] G. Gao, A.P. O'Mullane, A. Du, 2D MXenes: a new family of promising catalysts for the hydrogen evolution reaction, ACS Catal. 7 (2016) 494–500.
[16] Y. Jiao, Y. Zheng, K.R. Davey, S. Qiao, Activity origin and catalyst design principles for electrocatalytic hydrogen evolution on heteroatom-doped graphene, Nat. Energy 1 (2016) 16130.
[17] Y. Zheng, Y. Jiao, Y. Zhu, L.H. Li, Y. Han, Y. Chen, A. Du, M. Jaroniec, S. Qiao, Hydrogen evolution by a metal-free electrocatalyst, Nat. Commun. 5 (2014) 3783.
[18] G. Gao, Y. Jiao, F. Ma, Y. Jiao, E. Waclawik, A. Du, Metal-free graphitic carbon nitride as mechano-catalyst for hydrogen evolution reaction, J. Catal. 332 (2015) 149–155.
[19] W. Zhou, J. Zhou, Y. Zhou, J. Lu, K. Zhou, L. Yang, Z. Tang, L. Li, S. Chen, N-doped carbon-wrapped cobalt nanoparticles on N-doped graphene nanosheets for high-efficiency hydrogen production, Chem. Mater. 27 (2015) 2026–2032.
[20] Z. Fang, L. Peng, Y. Qian, X. Zhang, Y. Xie, J.J. Cha, G. Yu, Dual tuning of Ni–Co–A (A = P, Se, O) nanosheets by anion substitution and holey engineering for efficient hydrogen evolution, J. Am. Chem. Soc. 140 (2018) 5241–5247.
[21] J. Wang, F. Li, X. Liu, H. Zhou, X. Shao, Y. Qu, M. Zhao, Cu$_3$N and its analogs: a new class of electrodes for lithium ion batteries, J. Mater. Chem. A 5 (2017) 8762–8768.
[22] G. Kresse, D. Joubert, From ultrasoft pseudopotentials to the projector augmented-wave method, Phys. Rev. B 59 (1999) 1758–1775.
[23] G. Kresse, J. Furthmuller, Efficient iterative schemes for ab initio total-energy calculations using a plane-wave basis set, Phys. Rev. B 54 (1996) 11169–11186.
[24] J.P. Perdew, K. Burke, Y. Wang, Generalized gradient approximation for the exchange-correlation hole of a many-electron system, Phys. Rev. B 54 (1996) 16533–16539.
[25] J.P. Perdew, K. Burke, M. Ernzerhof, Generalized gradient approximation made simple, Phys. Rev. Lett. 77 (1996) 3865–3868.
[26] J. Heyd, G.E. Scuseria, M. Ernzerhof, Hybrid functionals based on a screened coulomb potential, J. Chem. Phys. 118 (2003) 8207–8215.
[27] D.J. Chadi, Special points for Brillouin-zone integrations, Phys. Rev. B 16 (1977) 1746–1747.
[28] S. Grimme, Semiempirical Gga-type density functional constructed with a long-range dispersion correction, J. Comput. Chem. 27 (2006) 1787–1799.
[29] G. Henkelman, B.P. Uberuaga, H. Jónsson, A climbing image nudged elastic band method for finding saddle points and minimum energy paths, J. Chem. Phys. 113 (2000) 9901–9904.
[30] G. Henkelman, H. Jónsson, Improved tangent estimate in the nudged elastic band method for finding minimum energy paths and saddle points, J. Chem. Phys. 113 (2000) 9978–9985.
[31] J. Rossmeisl, Z.W. Qu, H. Zhu, G.J. Kroes, J.K. Nørskov, Electrolysis of water on oxide surfaces, J. Electroanal. Chem. 607 (2007) 83–89.
[32] J. Rossmeisl, A. Logadottir, J.K. Nørskov, Electrolysis of water on (oxidized) metal surfaces, Chem. Phys. 319 (2005) 178–184.
[33] H. Xu, D. Cheng, D. Cao, X.C. Zeng, A universal principle for a rational design of single-atom electrocatalysts, Nat. Catal. 1 (2018) 339–348.
[34] P. Ehrlich, G. Pietzka, Über Titantrifluorid, Z. Anorg. Allg. Chem. 275 (1954) 121–140.
[35] K. Vorres, J. Donohue, The structure of titanium oxydifluoride, Acta Crystallogr. 8 (1955) 25–26.
[36] B.J. Kennedy, T. Vogt, Power X-ray diffraction study of the rhombohedral to cubic phase transition in TiF$_3$, Mater. Res. Bull. 37 (2002) 77–83.
[37] K. Meisel, Rheniumtrioxyd. Über Die Kristallstruktur Des Rheniumtrioxyds, Z. Anorg. Allg. Chem. 207 (1932) 121–128.
[38] L.S. Palatnik, O.A. Obol'yaninova, M.N. Naboka, N.T. Gladkikh, New modifications of tungsten oxides, Inorg. Mater. 9 (1973) 801–804.
[39] P. Ehrlich, F. Plöger, G. Pietzka, Über Niobtrifluorid, Z. Anorg. Allg. Chem. 282 (1955) 19–23.
[40] V. Gutman, K. Jack, The crystal structures of molybdenum trifluoride, MoF$_3$, and tantalum trifluoride, TaF$_3$, Acta Crystallogr. 4 (1951) 244–246.
[41] P. Fedorov, B. Sobelev, V. Trncova, Ionic conductivity and dielectric relaxation of

scandium fluoride, Crystallogr. Rep. 40 (1995) 663–666.

[42] X. Meng, B. Huang, X. Ma, Z. Wang, Z. Zheng, J. Wang, X. Qin, X. Zhang, Y. Dai, A Ti^{3+}:TiO_2/TiF_3 hybrid with enhanced visible-light photocatalytic reactivity, CrystEngcomm 16 (2014) 6538–6541.

[43] R.R. Shahi, A. Bhatnagar, S.K. Pandey, V. Dixit, O.N. Srivastava, Effects of Ti-based catalysts and synergistic effect of Swcnts-TiF_3 on hydrogen uptake and release from MgH_2, Int. J. Hydrog. Energy 39 (2014) 14255–14261.

[44] J. Wang, F. Li, B. Yang, X. Liu, M. Zhao, Half-metallic TiF_3: a potential anode material for Li-ion spin batteries, J. Mater. Chem. A 5 (2017) 21486–21490.

[45] G. Henkelman, A. Arnaldsson, H. Jonsson, A fast and robust algorithm for Bader decomposition of charge density, Comput. Mater. Sci. 36 (2006) 354–360.

[46] J.K. Norskov, T. Bligaard, A. Logadottir, J.R. Kitchin, J.G. Chen, S. Pandelov, U. Stimming, Trends in the exchange current for hydrogen evolution, J. Electrochem. Soc. 152 (2005) J23–J26.

[47] J.K. Norskov, T. Bligaard, J. Rossmeisl, C.H. Christensen, Towards the computational design of solid catalysts, Nat. Chem. 1 (2009) 37–46.

[48] Y. Wang, L. Chen, X. Yu, Y. Wang, G. Zheng, Superb alkaline hydrogen evolution and simultaneous electricity generation by Pt-decorated Ni_3N nanosheets, Adv. Energy Mater. 7 (2017) 1601390.

[49] R. Kavian, S. Choi, J. Park, T. Liu, H.C. Peng, N. Lu, J. Wang, M.J. Kim, Y. Xia, S.W. Lee, Pt–Ni octahedral nanocrystals as a class of highly active electrocatalysts toward the hydrogen evolution reaction in an alkaline electrolyte, J. Mater. Chem. A 4 (2016) 12392–12397.

[50] A. Oh, Y.J. Sa, H. Hwang, H. Baik, J. Kim, B. Kim, S.H. Joo, K. Lee, Rational design of Pt-Ni-Co ternary alloy nanoframe crystals as highly efficient catalysts toward the alkaline hydrogen evolution reaction, Nanoscale 8 (2016) 16379–16386.

[51] S.A. Abbas, S.H. Kim, M.I. Iqbal, S. Muhammad, W.S. Yoon, K.D. Jung, Synergistic effect of nano-Pt and Ni spine for her in alkaline solution: hydrogen spillover from nano-Pt to Ni spine, Sci. Rep. 8 (2018) 2986.

[52] L. Huang, Y. Hou, Z. Yu, Z. Peng, L. Wang, J. Huang, B. Zhang, L. Qian, L. Wu, Z. Li, Pt/Fe-NF electrode with high double-layer capacitance for efficient hydrogen evolution reaction in alkaline media, Int. J. Hydrog. Energy 42 (2017) 9458–9466.

[53] B. Hammer, J.K. Norskov, Theoretical surface science and catalysis: calculations and concepts, Adv. Catal. 45 (2000) 71–129.

[54] W. Pei, S. Zhou, Y. Bai, J. Zhao, N-doped graphitic carbon materials hybridized with transition metals (compounds) for hydrogen evolution reaction: understanding the synergistic effect from atomistic level, Carbon 133 (2018) 260–266.